



**NAVAL
POSTGRADUATE
SCHOOL**

MONTEREY, CALIFORNIA

THESIS

**THERMOMECHANICAL CYCLING INVESTIGATION OF CU
PARTICULATE AND NITI REINFORCED LEAD-FREE
SOLDER**

by

W. Scott Horton

September 2006

Thesis Advisor:

Indranath Dutta

Approved for public release; distribution is unlimited

THIS PAGE INTENTIONALLY LEFT BLANK

REPORT DOCUMENTATION PAGE			Form Approved OMB No. 0704-0188	
Public reporting burden for this collection of information is estimated to average 1 hour per response, including the time for reviewing instruction, searching existing data sources, gathering and maintaining the data needed, and completing and reviewing the collection of information. Send comments regarding this burden estimate or any other aspect of this collection of information, including suggestions for reducing this burden, to Washington headquarters Services, Directorate for Information Operations and Reports, 1215 Jefferson Davis Highway, Suite 1204, Arlington, VA 22202-4302, and to the Office of Management and Budget, Paperwork Reduction Project (0704-0188) Washington DC 20503.				
1. AGENCY USE ONLY (Leave blank)		2. REPORT DATE September 2006	3. REPORT TYPE AND DATES COVERED Master's Thesis	
4. TITLE AND SUBTITLE: Thermomechanical Cycling Investigation of Cu and Niti Reinforced Lead-Free Solder			5. FUNDING NUMBERS	
6. AUTHOR(S) W. Scott Horton				
7. PERFORMING ORGANIZATION NAME(S) AND ADDRESS(ES) Naval Postgraduate School Monterey, CA 93943-5000			8. PERFORMING ORGANIZATION REPORT NUMBER	
9. SPONSORING /MONITORING AGENCY NAME(S) AND ADDRESS(ES) N/A			10. SPONSORING/MONITORING AGENCY REPORT NUMBER	
11. SUPPLEMENTARY NOTES The views expressed in this thesis are those of the author and do not reflect the official policy or position of the Department of Defense or the U.S. Government.				
12a. DISTRIBUTION / AVAILABILITY STATEMENT Approved for public release; distribution is unlimited			12b. DISTRIBUTION CODE	
13. ABSTRACT (maximum 200 words) In today's Flip Chip (FC) and Ball Grid Array (BGA) electronic packages solder joints provide both the electrical as well as the mechanical connections between the silicon chip and the substrate. Due to coefficient of thermal expansion (CTE) differences between the chip and substrate the solder joints undergo thermomechanical stresses and strains as an electronic package is heated and cooled with power on/off cycles. Advances in chip designs result in chips that are larger, run hotter and demand improved resistance to creep and low-cycle fatigue in the solder joints. In this study the strengthening of these joints with two different reinforcements is explored: a hard particulate and a shape memory alloy (SMA) single fiber composite (SFC). A baseline is established with a SnAgCu solder that is then compared to test runs on the same solder matrix with Copper particles and then the SMA, Nickel-Titanium wire as reinforcements.				
14. SUBJECT TERMS Shape Memory Alloy, Thermomechanical Cycling, Lead Free Solder, Particulate Reinforcement, Active Reinforcement			15. NUMBER OF PAGES 75	
			16. PRICE CODE	
17. SECURITY CLASSIFICATION OF REPORT Unclassified	18. SECURITY CLASSIFICATION OF THIS PAGE Unclassified	19. SECURITY CLASSIFICATION OF ABSTRACT Unclassified	20. LIMITATION OF ABSTRACT UL	

THIS PAGE INTENTIONALLY LEFT BLANK

Approved for public release; distribution is unlimited

**THERMOMECHANICAL CYCLING INVESTIGATION OF CU PARTICULATE
AND NITI REINFORCED LEAD-FREE SOLDER**

W. Scott Horton
Lieutenant Commander, United States Navy
B.S., Purdue University, 1996

Submitted in partial fulfillment of the
requirements for the degree of

MASTER OF SCIENCE IN MECHANICAL ENGINEERING

from the

**NAVAL POSTGRADUATE SCHOOL
September 2006**

Author: W. Scott Horton

Approved by: Indranath Dutta
Thesis Advisor

Tony Healey
Chairman, Department of Mechanical and
Astronautical Engineering

THIS PAGE INTENTIONALLY LEFT BLANK

ABSTRACT

In today's Flip Chip (FC) and Ball Grid Array (BGA) electronic packages solder joints provide both the electrical as well as the mechanical connections between the silicon chip and the substrate. Due to coefficient of thermal expansion (CTE) differences between the chip and substrate the solder joints undergo thermomechanical stresses and strains as an electronic package is heated and cooled with power on/off cycles. Advances in chip designs result in chips that are larger, run hotter and demand improved resistance to creep and low-cycle fatigue in the solder joints. In this study the strengthening of these joints with two different reinforcements is explored: a hard particulate and a shape memory alloy (SMA) single fiber composite (SFC). A baseline is established with a SnAgCu solder that is then compared to test runs on the same solder matrix with Copper particles and then the SMA, Nickel-Titanium wire as reinforcements.

THIS PAGE INTENTIONALLY LEFT BLANK

TABLE OF CONTENTS

I.	INTRODUCTION	1
II.	BACKGROUND	5
A.	SOLDER	5
1.	Solder in Microelectronic Devices	6
2.	Thermomechanical Behavior	7
3.	Lead-Free Solder	9
B.	NITI - SHAPE MEMORY ALLOY	13
1.	SMA In Commercial Fields	14
2.	Basics of the Shape Memory Effect	15
III.	OBJECTIVES	19
IV.	EXPERIMENTAL PROCEDURES	21
A.	MATERIAL FABRICATION	21
B.	BALL SJS JOINTS	24
C.	CYLINDRICAL SJS JOINTS	28
D.	APPARATUS FOR TMC	31
E.	DATA AND EQUATIONS	34
F.	MICROSCOPIC OBSERVATION	36
V.	RESULTS AND CONCLUSIONS	39
A.	THERMOMECHANICAL CYCLING	39
B.	DIFFERENTIAL SCANNING CALORIMETRY	43
C.	SHAPE MEMORY EFFECT	46
D.	MICROSTRUCTURE	48
VI.	SUMMARY	53
	LIST OF REFERENCES	55
	INITIAL DISTRIBUTION LIST	59

THIS PAGE INTENTIONALLY LEFT BLANK

LIST OF FIGURES

Figure 1.	Cross-Section of a circuit board with FC and BGA constituents.....	1
Figure 2.	Examples of solder joining using (a) through-hole, (b) wire-bonding and (c) FC and BGA surface mounting.....	7
Figure 3.	FC or BGA solder balls under shear.....	8
Figure 4.	Sn-Ag-Cu tertiary showing Sn-rich matrix and intermetallic inclusions.....	13
Figure 5.	The initial soft twinned martensite NiTi structure in lower left, then shown deformed after loading. Following heating the structure transforms to austenite and recovers the original shape. Finally, when cooled the material transforms back to the twinned martensite structure.....	17
Figure 6.	(a) Argon chamber; (b) Cup and mixing blade for mixing copper into solder.....	22
Figure 7.	(a) Picture and (b) schematic of rod for ball-type joint following vapor deposit with bond pad exposed.....	25
Figure 8.	(a) Schematic and (b) picture of furnace and fixture for manufacture of SJS ball-type joint. The structure and fixture were cut from 7000 series aluminum. Additional insulation was placed over the top and front but is not seen in this figure.....	26
Figure 9.	(a) Picture and (b) schematic of completed SJS ball-type joint.....	28
Figure 10.	(a) Picture and (b) schematic of Cu rod used in cylinder-type joints. (c) and (d) show the assembled cylinder-type joint.....	29
Figure 11.	(a) Schematic and (b) picture of mold and C-shapes for cylinder-type joint.....	30
Figure 12.	(a) schematic and (b) picture of the Thermomechanical Cycling Apparatus.....	32
Figure 13.	Bimetallic loading frame.....	33
Figure 14.	a) $\bar{\tau}$ vs. T, b) $\bar{\gamma}$ vs. T. for the 12 th cycle of the monolith and Cu reinforced ball-type SJS joints.....	40
Figure 15.	a) $\bar{\tau}$ vs. T, b) $\bar{\gamma}$ vs. T. for the 12 th cycle of the monolith and SFC reinforced cylindrical-type SJS joints.....	41

Figure 16.	a) $\bar{\tau}$ vs. T, b) $\bar{\gamma}$ vs. T. for the 1 st cycle of the monolith and SFC reinforced cylindrical-type SJS joints.....	42
Figure 17.	Two DSC scans of NiTi samples over dissimilar temperature ranges.....	44
Figure 18.	$\bar{\gamma}_{inelastic}$ vs. T for 1 st and 12 th cycles of SFC over limited range.....	48
Figure 19.	SnAgCu SJS ball joint (a) overview, (b) & (c) microstructure after 48 TMC at 750X and 3000X...	49
Figure 20.	SnAgCu microstructure after 96 TMC, (a) 1500X, (b) 3000X.....	50
Figure 21.	Cu/Cu ₆ Sn ₅ reinforced ball-type SJS joints under magnification. (a) Cu/Cu ₆ Sn ₅ conversion at interfaces, (b) uniform dispersion of reinforcements within matrix, (c) reinforcements located at the matrix grain boundaries.....	51
Figure 22.	NiTi SFC reinforced cylindrical-type SJS joints. (a) solder matrix, (b) Ni ₃ Sn ₄ layer formed at the interface of the SFC and matrix...	51

LIST OF TABLES

Table 1.	Elemental composition of lead-free solders.	
	[15].....	13

THIS PAGE INTENTIONALLY LEFT BLANK

ACKNOWLEDGMENTS

The author gratefully acknowledges the financial support of this investigation by the Army Research Office under grant Nr 42714MA, with Dr. David Stepp as program monitor.

I would like to express my sincere gratitude and appreciation to Professor Indranath Dutta for his guidance and patience during the work in performing this investigation. I am also indebted to Tom Christian, Dr. Deng Pan and LT William Wright.

Most of all, I would like to thank my wife, Mrs. Joan Carney Horton. Without her support and encouragement at home this study would not have been possible.

THIS PAGE INTENTIONALLY LEFT BLANK

I. INTRODUCTION

In the Flip Chip (FC) and Ball Grid Array (BGA) microelectronic architectures solder balls are the electrical and mechanical connections between the silicon chip and the substrate. Figure 1 shows such a Flip Chip On Board (FCOB) device that consists of a FC/BGA device. In each case a dense array of solders balls resides between two materials of differing Coefficient of Thermal Expansion (CTE). As the device thermodynamically cycles with each on/off power cycle, stress and strain are placed upon the solder ball connections by the differing expansions of the materials they connect. Solder balls are thermomechanically cycled this way at high homologous temperatures resulting in activated high temperature creep mechanisms and low cycle fatigue failures.

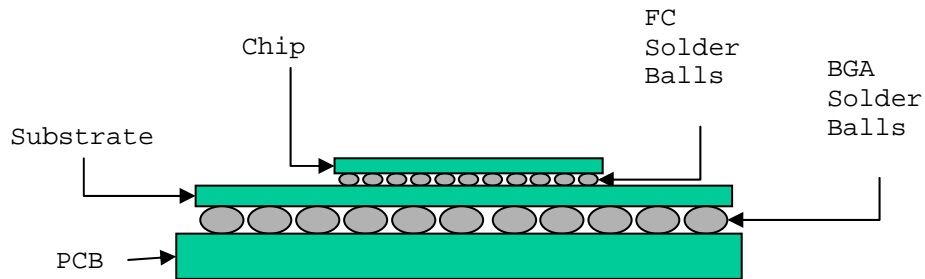


Figure 1. Cross-Section of a circuit board with FC and BGA constituents.

In the future, the demands placed on the solder balls will be even greater. The International Technology Roadmap for Semiconductors (ITRS) [1] specifically says the temperatures will increase 20°C to 175°C, the chip size will increase 5 to 25 mm. The most telling of future demands is the package pin count will increase to 3158 from

2007. This correlates to an increase in solder joint density per unit area, and will necessitate a decrease in solder ball size.

An increase in operating temperature will exacerbate the difference in CTE to place a greater stress/strain on the solder ball that is now already operating at a high homologous temperature. If current solders are used the creep and low-cycle fatigue will only become more significant. This is why composite solders are studied here. Lead-free solders as mandated by legislation are not in themselves a great improvement over Lead-Tin, composite technology is looked upon to provide the boost in creep resistance and strength needed to survive in future microelectronic package environments.

In this study two types of composites are examined: a Cu/Cu₆Sn₅ particulate reinforcement and a NiTi shape memory alloy (SMA) single fiber composite (SFC). The Cu/Cu₆Sn₅ reinforcement has been studied elsewhere [2-5] but is used here to make a direct comparison between the effects of passive and active reinforcements using identical equipment and methods.

The active reinforcement SMA is incorporated into the solder in the form of a 1 mm diameter wire in order to explore the usefulness of the shape memory effect in solder applications. The SMA fiber used is martensitic at room temperature. When heated in thermomechanical cycling (TMC) the temperature will be elevated above the austenitic transformation temperature of the SMA. At this transformation temperature the SMA will be able to not only resist strain but will exhibit a reversing force as the SMA

attempts to regain its initial shape. The reversal will alleviate strain in the solder, extending the life cycle of the solder joint.

The objective of this study is to examine qualitatively the effects of the passive and active reinforcements during TMC.

THIS PAGE INTENTIONALLY LEFT BLANK

II. BACKGROUND

A. SOLDER

Solder is the prime method of electrical connection and in modern microelectronic device architectures it is also the structural connection between the silicon chips and printed circuit boards. In recent ball grid arrays it is also an important surface for heat dissipation.

For decades lead-tin solders have been the staple and they have been studied extensively and their properties are understood on a comprehensive level. The two factors generally thought to be most important to solder joint reliability are creep resistance and thermomechanical fatigue resistance [5-12]. These properties in Pb-Sn solders have been studied and modeled by numerous persons and information is readily available. As modern time moves the industry towards lead-free solders these solders will be the focus of fervent study and development of models to accurately predict their behaviors is a priority.

In addition to new lead-free alloys, composite solders are being studied. Ideally, manufacturing a composite would result in a material with the desired properties much improved from either the matrix or reinforcement. Numerous reinforcements have already been studied using both Pb-Sn and lead-free solder matrices. Hard particulates such as Ag, Cu, Cu_6Sn_5 , and Ni are examples that have received attention, with positive reports of improved characteristics vs. the non-reinforced solder base [2-5]. A new direction has recently been taken with the study of materials that would be adaptive to the stresses

experienced. These materials are Shape Memory Alloys (SMA), NiTi is one such SMA studied in this paper.

1. Solder in Microelectronic Devices

Solder has been used for years to connect devices electrically using through-hole and wire bond solder joints. Flip-chip (FC) and ball-grid array (BGA) surface mount architectures have added the burden of mechanical connection to the functions of solder. In these devices the solder balls must connect a silicon chip to a printed circuit board with no other means of connection. That requirement in this environment can be brutal for solder where temperatures can be in excess of two thirds of the homologous temperature.

Through-hole and wire-bond soldering have traditionally been the norm. As the pitch of connections is reduced the wires must be reduced in size accordingly, resulting in thinner and more flexible wire. The problem of sweep and deflection becomes increasingly more exaggerated. With the advent of FC and BGA architectures an advanced soldering connection is provided. Figures 2 (a-c) show the different soldering methods in profile. The obvious difference is the elimination of the wire. Using surface mount architecture eliminates the wire altogether and with that has solved the problems of increased sweep and deflection.

In number of inputs/outputs (I/O) is where the surface mount architectures far surpass even the most advanced wire-bond methods. The area array of solder balls provides for extremely dense patterns of I/O connections. In addition to sheer number of I/O's the length of interconnect is minimized and thus the inductance is

minimized. For this reason surface mount architectures are used where clock speed is to be maximized. Also, as a result of the dense I/O arrays and short interconnects, the surface mount architectures are physically smaller than devices with wire-bond interconnects with similar numbers of I/O's. Hence, surface mount architectures are the structure of choice in size critical applications such as cellular phones or hand held computers.

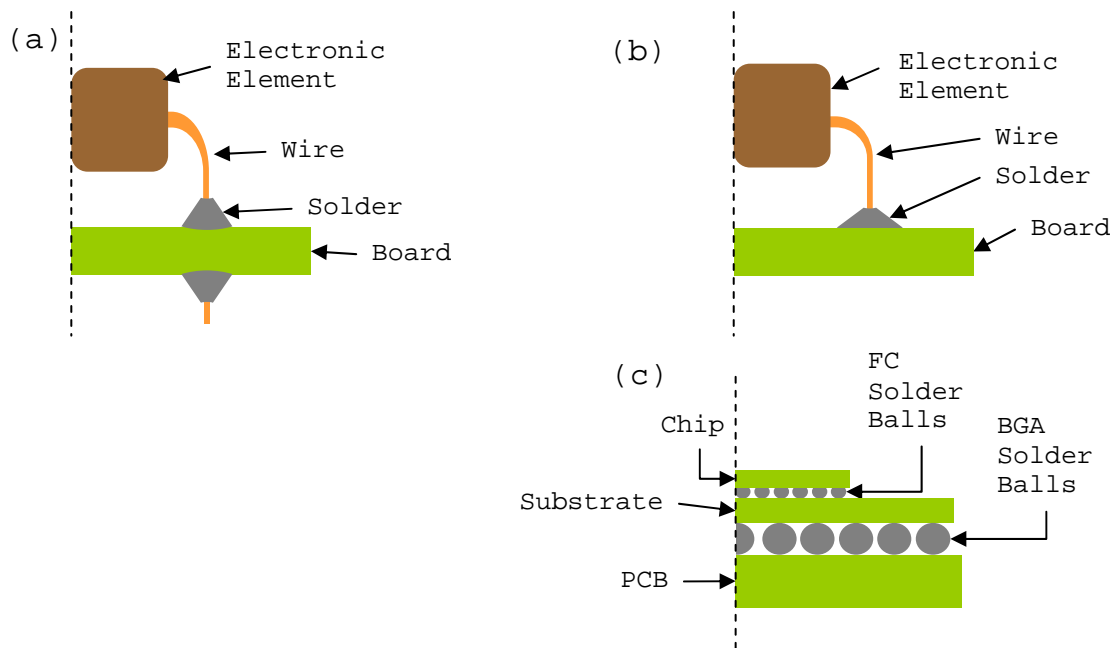


Figure 2. Examples of solder joining using (a) through-hole, (b) wire-bonding and (c) FC and BGA surface mounting.

2. Thermomechanical Behavior

The new problem presented with the surface mount technologies is low cycle fatigue (LCF) of the solder balls. This LCF is induced by thermomechanical cyclic shear stresses at high homologous temperatures that occur with each on/off cycle of the device. The shear stresses are a result of the coefficient of thermal expansion (CTE)

difference between the chip and the substrate. FR-4, a commonly used epoxy-glass PCB substrate [24], has a CTE of $18.5 \times 10^{-6}/\text{K}$ [13] vice Si where $\text{CTE} = 2.8 \times 10^{-6}/\text{K}$ [13]. This difference of more than 660% means the chip and substrates will experience vastly different lengths of thermal expansion, and with solder being the softest member of the device it will have to absorb these cyclical shear forces. The shear forces result in accumulated inelastic strains that lead to the low cycle fatigue that can eventually result in the failure of the device. Figure 3 shows the geometry of a surface mount architecture at operating temperature.

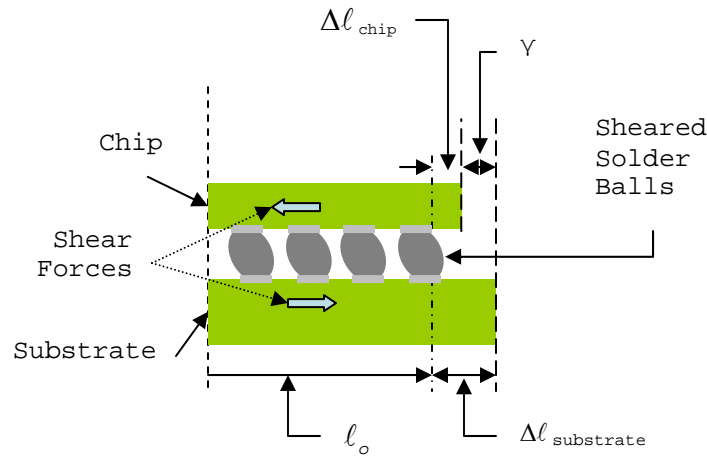


Figure 3. FC or BGA solder balls under shear.

Operating at high homologous temperatures, T_H , (0.6 - 0.8) allows the solder to participate in thermally activated processes. Grain growth and creep are such processes. At this sufficiently high T_H any application of stress and creep is to be expected. Now, combine the high T_H with the induced stresses and significant strain-enhanced grain coarsening is the result. It has been found that

this grain coarsening has a tremendous effect on the reliability of the solder joints. Experiments on Pb-Sn solder demonstrated that the measured fatigue life with grain coarsening was only 21 percent of the expected if no grain coarsening had occurred [9]. It is desired that new lead-free solders will alleviate this problem somewhat. The grains in Pb-Sn solders are typically equal mixes of Pb-rich and Sn-rich phases, whereas in Sn-Ag or Sn-Ag-Cu there is a Sn matrix with dispersed particles of Ag and Cu intermetallics. When the Pb-Sn solder coarsens both phases coarsen, much different from the lead-free solders where only the intermetallics grow within the Sn matrix. The variance in coarsening between the two solders results in different creep mechanisms being promoted. The phase coarsening of Pb-Sn finds its effects in diffusion creep and is greatly affected by the TMC [7], converse to Sn-Ag or Sn-Ag-Cu solders that are thought to be affected more by dislocation creep and the coarsening of the intermetallics. This coarsening is well understood in the Pb-Sn solders, well enough that models of failure have been developed that take the coarsening into account [8, 9]. The lead-free solders with their different phase structure require more research in order to develop a model for estimation of joint reliability.

3. Lead-Free Solder

To date the most prolific solder has been Pb-Sn alloy. Recent legislation [14] and worldwide pressure to eliminate the toxicity of the heavy metal Pb has forced industries to look for a 'green' replacement. The perfect replacement needs to have excellent properties in two regions, one is performance and reliability, the other is relevant to manufacturing. Performance and reliability is affected by

things such as electrical conductivity, thermal conductivity, CTE, resistance to creep, etc. Manufacturing concerns include wettability, environmental friendliness, ability to be made into balls or paste, etc. Another important manufacturing concern is the similarity of the solderability to the current staple. If proposed solders are too dissimilar in solderability there would be the need for development of new processes and possibly new materials for chip and substrate [15]. However, despite the important properties above, perhaps the most important property of the replacement solder is cost. Even the 'perfect' solder would be useless if its materials cost was prohibitive, exemplified by alloys using Indium. Though alloys using Indium have been used in some FC applications where they have demonstrated promising results, they may not see wide scale use in industry as a leaded solder replacement, because their cost has been variable and high.

There are numerous alloys that have been studied or proposed using materials Sn, Bi, In, Cu, Ag, Zn, Sb, Fe, and even Pb. As seen in Table 1 [15], nearly all lead-free solders in development use Sn as the major constituent, though Bi and In matrix variants have also been developed. The most common variants in research literature are SnAg and SnAgCu though variants of Bi and In are also available in industry.

The solder with Bi and In matrix are now commonplace, primarily in low temperature uses due to their usually lower liquidous temperature [15]. In has been used in FC applications but it is not an ideal replacement for numerous reasons. One being its low melting temperature but more importantly is the cost and supply of In are both

variable. The cost of In is nominally higher than other possible elements, but the price is variable too, which could prove to be a problem for a manufacturer seeking consistency. The availability of In is another issue. There are no In mines, it is taken as a by-product of Sn or Pb production. This equates to low production rates with no predicted increase. The demand for In, however, has increased in recent years. The highest demand for In is in thin films, most predominately in flat screen LCD monitors. This is a demand that is growing. For these reasons alone In is not the ideal Pb substitute.

The solder variants using a Sn matrix and differing amounts of Ag or Ag and Cu have received much attention in research, to include composite solder research [3-5, 24-26]. The reviews are consistently the most favorable as a Pb-Sn replacement, exemplified by the National Electronics Manufacturing Initiative (NEMI) press release in January, 2000, recommending $\text{Sn}_{3.9}\text{Ag}_{0.6}\text{Cu}$ for 70% of soldering tasks [16]. Therefore, alloys of this ternary system have received the most study, including this paper.

Alloys	Sn	In	Zn	Ag	Bi	Sb	Cu	Mg	Fe	Pb
Sn-37Pb	63									37
Sn-40Pb	60									40
Bi-26In-17Sn	17	26			57					
Bi-32In		32			68					
Bi-41.7Sn-1.3Zn	41.7		1.3		57					
Bi-41Sn-1Ag	41			1	58					
Bi-41Sn-1Pb	41				58					1
Bi-42Sn	42				58					
Bi-43Sn (eutectic)	43				57					
Bi-43Sn+2.5% Fe	43				54.5				2.5	
Bi-45Sn-0.33Ag	45			0.33	54.7					
In-3Ag		97		3						
In-34Bi		66			34					
In-48Sn (eutectic)	48	52								
Sn-1Ag-1Sb	98			1		1				
Sn-1Ag-1Sb-1Zn	97		1	1		1				
Sn-2.5Ag-0.8Cu-0.5Sb	96.2			2.5		0.5	0.8			
Sn-2.8Ag-20In	77.2	20		2.8						
Sn-25Ag-10Sb	65			25		10				
Sn-2Ag	98			2						
Sn-2Ag-0.8Cu-0.6Sb-(CASTIN)	96.6			2		0.6	0.8			
Sn-2Ag-0.8Cu-6Zn	91.2		6	2			0.8			
Sn-2Ag-0.8Cu-8Zn	89.2		8	2			0.8			
Sn-3.5Ag	96.5			3.5						
Sn-3.5Ag-6Bi	90.5			3.5	6					
Sn-3.5Ag-1Zn	95.5		1	3.5						
Sn-3.5Ag-1Zn-0.5Cu	95		1	3.5			0.5			
Sn-3.6Ag-1.5Cu	94.9			3.6			1.5			
Sn-4.7Ag-1.7Cu	93.6			4.7			1.7			
Sn-4Ag	96			4						
Sn-4Ag-7Sb	89			4		7				
Sn-4Ag-7Sb-1Zn	88		1	4		7				
Sn-10Bi-0.8Cu	89.2				10		0.8			
Sn-10Bi-0.8Cu-1Zn	88.2		1		10		0.8			
Sn-10Bi-5Sb	85				10	5				
Sn-10Bi-5Sb-1Zn	84		1		10	5				
Sn-4.8Bi-3.4Ag	91.8			3.4	4.8					
Sn-42Bi	58				42					
Sn-45Bi-3Sb	52				45	3				
Sn-45Bi-3Sb-1Zn	51		1		45	3				
Sn-56Bi-1Ag	43			1	56					
Sn-57Bi-1.3Zn	41.7		1.3		57					
Sn-5Bi-3.5Ag	91.5			3.5	5					
Sn-7.5Bi-2Ag-0.5Cu	90			2	7.5		0.5			
Sn-0.75Cu	99.25						0.75			
Sn-0.7Cu (eutectic)	99.3						0.7			
Sn-2Cu-0.8Sb-0.2Ag	97			0.2		0.8	2			
Sn-3Cu	97						3			
Sn-4Cu-0.5Ag	95.5			0.5			4			
Sn-10In-1Ag-(0-10.5)Bi	78.5	10		1	10.5					
	89	10		1	0					
Sn-20In-2.8Ag	77.2	20		2.8						
Sn-42In	58	42								
Sn-5In-3.5Ag	91.5	5		3.5						
Sn-10In-1Ag-0.5Sb	88.5	10		1		0.5				
Sn-36In	64	36								
Sn-50In	50	50								

Alloys	Sn	In	Zn	Ag	Bi	Sb	Cu	Mg	Fe	Pb
Sn-8.8In-7.6Zn	83.6	8.8	7.6							
Sn-2Mg (eutectic)	98							2		
Sn-5Sb	95					5				
Sn-4Sb-8Zn	88		8			4				
Sn-7Zn-10In-2Sb	81	10	7			2				
Sn-8Zn-10In-2Bi	80	10	8		2					
Sn-8Zn-4In	88	4	8							
Sn-8Zn-5In-(0.1-0.5)Ag	86.5	5	8	0.5						
Sn-9Zn-10In	81	10	9							
Sn-5.5Zn-4.5In-3.5Bi	86.5	4.5	5.5		3.5					
Sn-6Zn-6Bi	88		6		6					
Sn-9Zn (eutectic)	91		9							
Sn-9Zn-5In	86	5	9							

Table 1. Elemental composition of lead-free solders. [15]

Alloys of the SnAg binary and SnAgCu ternary have remarkably similar microstructures. A β -Sn matrix with small eutectic grains of Ag_3Sn rod-like intermetallics are identical in both the binary and ternary. The only difference being finely dispersed particles of Cu intermetallics throughout the grains of the tertiary.

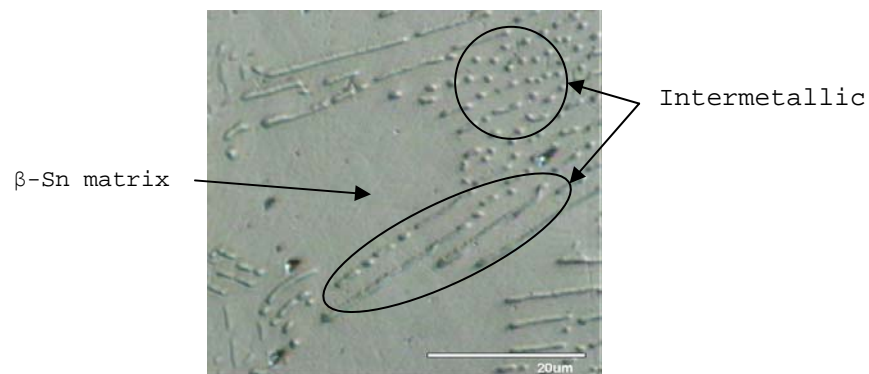


Figure 4. Sn-Ag-Cu tertiary showing Sn-rich matrix and intermetallic inclusions

B. NITI - SHAPE MEMORY ALLOY

Shape memory effect is the term used to describe the ability of a material to return to an initial pre-deformed shape following thermal activation. After brief 'discoveries' into the shape memory effect in the 1930's

through 50's, the breakthrough came in the 1960's by Buehler and co-workers at the Naval Ordinance Laboratories [17]. Their discovery of the shape memory effect was in an equiatomic nickel-titanium compound that became known as Nitinol (Nickel-Titanium Naval Ordinance Laboratory). In the years since, shape memory alloys (SMA) have received much attention and are now common in numerous fields.

1. SMA In Commercial Fields

Of the varying alloys that demonstrate shape memory, NiTi is one of the two alloy systems being pursued commercially, copper based alloys being the other. Both systems have their advantages and disadvantages that must be weighed for each application. The NiTi alloys are more thermally stable, have superior corrosion resistance and resistance to stress-corrosion cracking, higher ductility and nearly double the shape memory strain (8% vs. 5%) [17]. Advantages of the copper based alloys include ease of manufacturing, wider range of transformation temperatures and perhaps most importantly, much lower cost.

In medical fields NiTi is used extensively. In Osteosynthesis bone plates are used to hold fractured bones together during the healing process. The SMA plates have proven to perform well. The shape memory effect places the bones in permanent compression effectively returning a break to a constant bone that promotes healing and quick recovery [18]. In surgical connections of organs NiTi staples and sutures are gaining in uses. Again, the shape memory effect is activated by body heat and is making difficult connections more positive in organs such as tubular digestive organs [19]. In robotics the challenge of accurately modeling human movement is being answered by

SMA. Small NiTi wires are used as synthetic 'muscle' in the bending of joints. The controlled bending of the wire 'muscles' by shape memory effect is effected by passing currents through the wires to create the needed heat for material transformation. A group at Rutgers University is taking this a step further and developing robot prosthetic devices using SMA technology [27].

Other uses of SMA's include hydraulic connections, glasses frames, bra underwires, fire safety valves, etc. [18]. In each case the attributes of the different alloys must be weighed to determine proper material selection. While NiTi could be an excellent choice based on its physical properties, its cost compared to Cu based alloys could be prohibitive in situations where the Cu alloy will perform acceptably.

2. Basics of the Shape Memory Effect

The shape memory effect referred to above is the ability of a material to be deformed at one temperature and then return to its original shape after a defined thermal procedure. Those materials that exhibit this effect are known as Shape Memory Alloys. Materials that are plastically deformed while below a transformation temperature and when heated above will regain their original shape are said to have 'one-way shape memory.' Materials that will undergo shape change during heating and cooling are said to have 'two-way shape memory.' The shape memory upon heating is generally more robust in that it yields greater strain recovery and generates more force upon changing shape [17].

At temperatures below the transformation temperature NiTi is a thermoelastic martensite that is relatively soft and easily plastically deformed by applying a stress. There are actually numerous variants of the martensite formed in close proximity. They are twin related to neighboring variants to form a herringbone structure. This structure is self-accommodating in that the numerous variants are self-eliminating. Glissile interfaces between variants will slip readily allowing the martensite to be deformed by applying low stresses. This little organized structure of the martensite results in a relatively soft material. By either twinning mechanisms or mobile interfaces the plastic deformation by low applied stresses can be significant.

In stark contrast to the martensite, the austenite structure of NiTi is rigid in its orientation. Where the martensite has little order and has many variants existing in close proximity, the austenite does not maintain multiple variants of differing orientation. The cubic structure of the austenite supports only one orientation and therefore must return to its original shape upon transformation. For NiTi this transformation is initiated by heating above a transformation temperature. Figure 5 illustrates the different stages of the shape memory effect in NiTi: initial twinned martensite, following plastic deformation, to where heat has initiated the transformation to austenite.

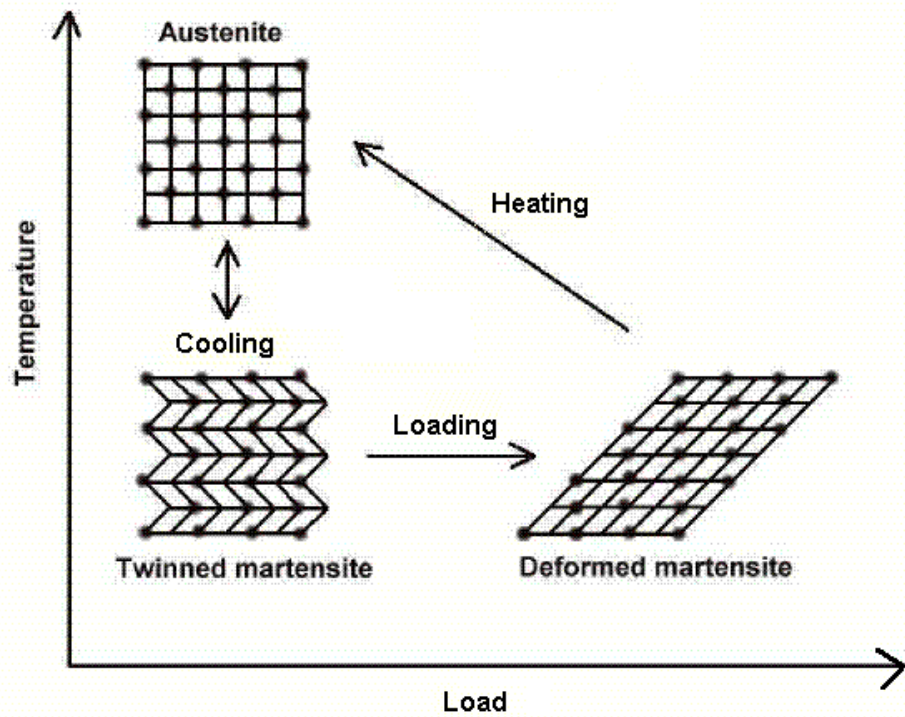


Figure 5. The initial soft twinned martensite NiTi structure in lower left, then shown deformed after loading. Following heating the structure transforms to austenite and recovers the original shape. Finally, when cooled the material transforms back to the twinned martensite structure.

THIS PAGE INTENTIONALLY LEFT BLANK

III. OBJECTIVES

As with the advancement in any technologies, multiple advancements must be made simultaneously for substantial strides to be made. In microelectronic devices, the introduction of lead-free solders has introduced a number of new challenges, one of the most critical is the reduced low-cycle fatigue life and reliability of lead-free surface mount joints. Older composites using conventional passive materials as reinforcements have been attempted before to improve reliability, but with limited success. The objective of this thesis is to explore the possibility of substantially enhancing the low-cycle fatigue life of lead-free solders by incorporating shape-memory alloy reinforcements in the solder. The thesis focuses on the fabrication and evaluation of model single fiber composite systems, as well as on the processing of particulate-containing systems.

THIS PAGE INTENTIONALLY LEFT BLANK

IV. EXPERIMENTAL PROCEDURES

A. MATERIAL FABRICATION

For ease of handling and to aid in consistency all soldering of joints was done with disk pre-forms. Disks of 3 mm diameter were punched out from a sheet of solder of known thickness. For the monolith samples, the process consisted of purchasing bulk 93.3Sn-3.0Ag-0.7Cu solder, then cold rolling it progressively thinner until a sheet 0.55 mm thick was obtained. The pre-form disks were then punched from the sheet and weighed to ensure consistency between samples. The process for the Cu/Cu₆Sn₅ reinforced solder was somewhat more lengthy.

The same bulk solder was used in manufacturing the Cu/Cu₆Sn₅ reinforced solder as in the monolith. Three large pieces of bulk solder were first cut from the monolith brick and reflowed into disks in the aluminum crucible seen in Figure 6b on a hot plate. The surfaces of each disk were sanded with silicon carbide paper to make both the upper and lower surfaces smooth and parallel with no large pits that could entrap air.

The copper used to reinforce the solder matrix was a spheroidal powder (<10 μ m). To eliminate agglomerates the copper powder was first ground with a mortar and pestle inside a chamber flooded with argon gas, Figure 6a. The powder was then weighed and an amount taken to provide for 7% by volume with respect to the solder. This quantity was then put back into the argon flooded chamber to be coated with flux. While mixing the copper powder by hand on a

glass dish with a spatula, drops of flux were slowly added until complete coverage of all copper particles was achieved; a thick copper paste was the desired result.

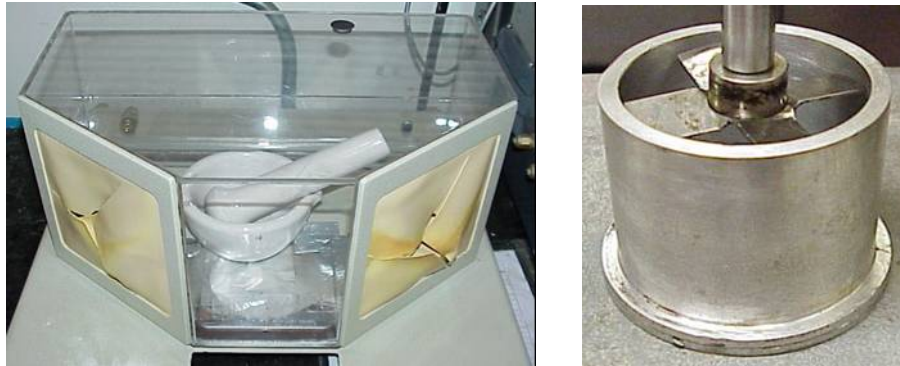


Figure 6. (a) Argon chamber; (b) Cup and mixing blade for mixing copper into solder.

To insert the copper into the solder a Cu-solder 'sandwich' was created in the aluminum crucible. The three solder disks were placed in the crucible with a layer of the copper paste between each disk. This was performed while under argon to negate air being trapped between the solder disks and oxygen being available to oxidize the copper when the 'sandwich' is heated. This was the reason the solder disks had been sanded smooth and pockets removed from the surface that might have held residual air. The crucible and its contents were then placed on the hot plate set at 250°C (523K). The crucible was placed in the center of an aluminum foil box structure erected on the hot plate to trap the argon during heating. The box's top was also foil with an access large enough for the glass tube supplying argon, mixing blade shaft and line of sight into the crucible. Early attempts had shown that the argon was necessary at all steps to prevent oxidation of the copper

particles. In practice, omission of argon during reflow did not just hinder copper admixture but nearly eliminated any copper from remaining within the solder.

To ensure uniform distribution of the copper throughout the solder matrix the composite was mechanically stirred after reflow on the hot plate for 15 minutes before cooling. A stainless steel mixing blade was file fit to the crucible for this purpose. The blades were fit to have minimal clearance with the sides of the crucible. This was to ensure minimal tip loss while stirring. It was observed in initial attempts that when a blade with a diameter significantly less, 3 mm, than the diameter of the crucible had been used, solder would cling to the wall of the crucible and thus, avoid mixture. With the custom fit blade this loss was eliminated.

After 15 minutes of mixing the crucible was immediately quenched in water and a solid cylinder of composite solder removed from the crucible. A portion of this solder was cut out and rolled into a sheet in the same fashion as the monolith. In all further steps the monolith and Cu/Cu₆Sn₅ reinforced composite solder were handled in an identical manner.

The Single Fiber Composite, SFC, reinforced solder pre-forms were assembled in a dissimilar process. The initial steps were performed at New Mexico Institute of Mining and Technology. The NiTi fiber was first prepared by annealing it for 30 minutes at 544°C (823K) to soften it. The surface was prepared with emery paper to remove oxides and then an HF-based flux (Indalloy flux Nr. 2, Indium Corporation of America) was used to coat the surface. The fiber was then placed in a mold aligned down

the central axis. Solder was reflowed into the mold and the resulting casting was a cylinder with the 1 mm diameter fiber as the central axis. This was the 'as delivered' condition to Naval Postgraduate School.

The cast SFC reinforced solder cylinder was then sectioned for further assembly into cylindrical joints. A diamond wafering saw was used to cut 3 mm long pre-forms to be used in joint assembly. Early samples that had not used the HF-based flux experienced separation of the fiber from the solder when cutting. The fiber would spin within the solder as the blade pressed against it or following cutting, the fiber would simply fall out of the solder cast. When cutting the HF-based flux treated samples no such difficulties were experienced. The resulting cylindrical pre-forms were then ready to be used in later steps of assembling the cylindrical SJS joints.

B. BALL SJS JOINTS

The first type of SJS joint tested was the ball type, so called because of the spherical shape the solder takes after reflow. This joint was used to simulate an up-scaled FC joint. For this joint two rods of copper were machined to 5.9 mm diameter by 19 mm in length. The bond pad was machined onto the center of one end by removal of the surrounding copper on a lathe. The pad was 1.6 mm diameter and raised 0.1 mm from the surrounding rod as shown in Figure 7a & 7b. Aluminum was vapor deposited onto this end surface, covering both pad and surrounding area. Thickness of the deposit was not measured, it was only necessary that coverage was complete. The aluminum, in this instance, functioned to protect the bond pads from building up oxides

while in storage. Pairs of rods were prepared to this stage then set aside for latter assembly into ball-type SJS joints.

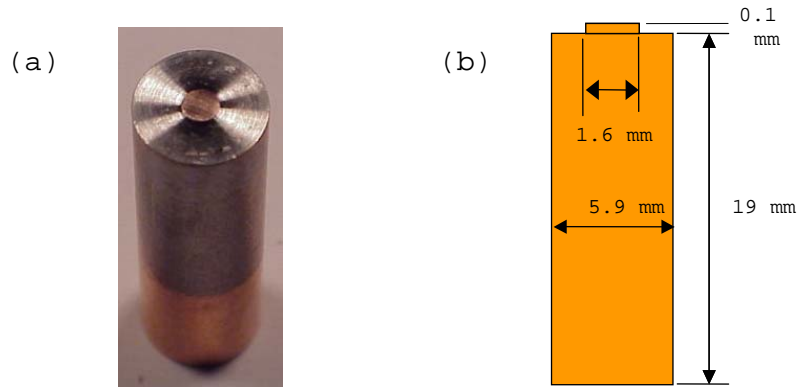


Figure 7. (a) Picture and (b) schematic of rod for ball-type joint following vapor deposit with bond pad exposed.

Just prior to assembling a ball-type joint the aluminum was removed from the bond pad with 1000 grit silicon carbide paper. The area surrounding the pad was left coated with aluminum to perform as solder masking. The end surface was visually inspected under magnification to ensure the pad surface was clear of aluminum and the surrounding area remained completely masked. Failure to completely remove the aluminum from the pad resulted in poor adhesion of the solder to the pad, or if the masking surrounding the pad had been removed an irregular shaped joint would result. The pads were then rubbed briefly with 4000 grit silicon carbide paper and rinsed with acetone followed by methanol. After the methanol was evaporated with cool air from a heat gun the pads were coated with flux.

To begin the assembly of the ball-type joint, the rods were first placed loosely in the fixture, Figure 8a inset, with bonding pads together. The fixture was then mounted in the furnace so the rods were resting on the anvil of the micrometer. The micrometer was zeroed and the upper rod fixed in position with setscrews. The micrometer thus controlled the position of the lower rod and, therefore, read the distance between the bond pads. Figures 8 (a & b) illustrate this apparatus. To manipulate the micrometer manually was not feasible inside the furnace so an electric motor, which was wired to a DC power supply, turned the micrometer via a shaft through the lower insulation of the furnace.

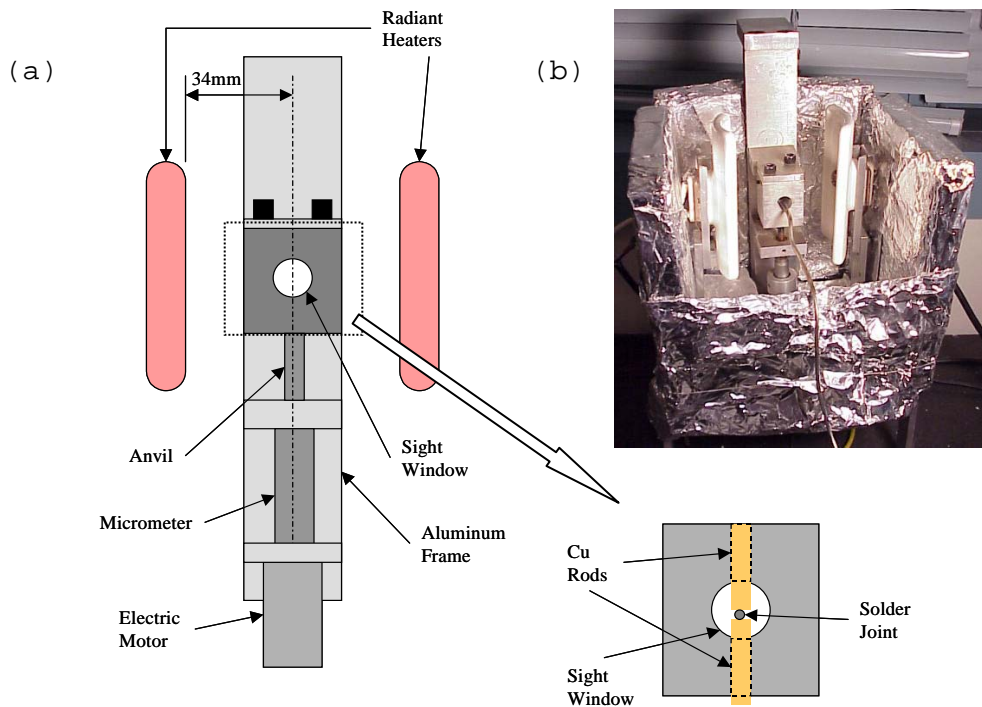


Figure 8. (a) Schematic and (b) picture of furnace and fixture for manufacture of SJS ball-type joint. The structure and fixture were cut from 7000 series aluminum. Additional insulation was placed over the top and front but is not seen in this figure.

The solder disks detailed in Section A of this chapter were then placed on the lower bond pad and the micrometer set to the thickness of the disks. The micrometer's motor was then 'bumped' until a noticeable strain on the electric motor was heard; this ensured that the solder disk was in firm contact with the bond pads. It was found that this step dramatically increased the reliability of the solder adhering to the upper bond pad. This step necessitated changing the drift pin on the motor shaft from brass to steel, as the additional bumping sheared brass drift pins.

Temperature inside the furnace was measured by a thermocouple pressed against the upper rod approximately 2-3 mm above the joint. The thermocouple was wired to the heater controller for the radiant heaters, thus controlling the temperature of the sample within the furnace. The furnace top and front insulation were then set in place with a small square left open in front for thermocouple passage and visuals of the solder joint and micrometer readings. The 500W 120VAC radiant heaters were controlled by a Eurotherm controller turned on to a set point of 260°C (533K) (as measured on the rod). Once the set point was reached and reflow of the solder achieved, the micrometer was slowly backed off to the desired joint height approximately 1.2 mm. A dwell time of 2 minutes was allowed at the final height before cooling began.

In order to cool the joint the heaters were turned off and the top and front insulation removed from the furnace. A heat gun was then used to blow cool air into the fixture's sight window and over the joint. The heat gun was positioned approximately 12 cm from the fixture in order to get a portion of the air to cool the surrounding

furnace structure as well. The initial cooling rate was approximately 10 K/sec. After 10 minutes of cooling the joint was removed from the fixture and was ready for testing. Figure 9 shows a completed ball-type SJS joint.

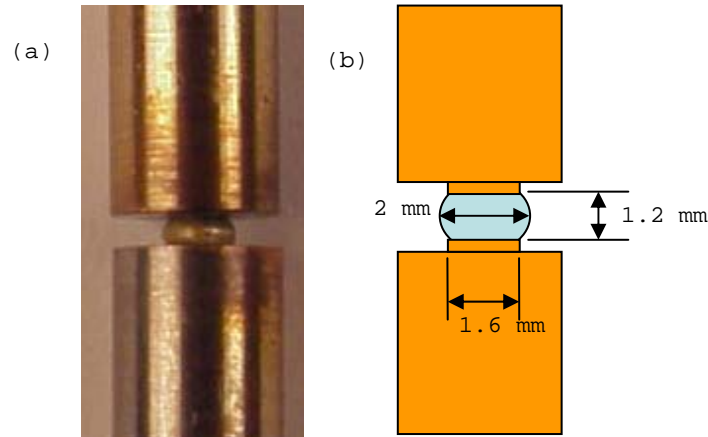


Figure 9. (a) Picture and (b) schematic of completed SJS ball-type joint.

C. CYLINDRICAL SJS JOINTS

The second type of joint tested was the cylindrical SJS joint. This joint did not model any joint in an electronic package but was used for comparison of materials only. In this joint copper rods were machined to 5.9 mm diameter by 19 mm in length, but no bonding pad was cut. In its place, a recessed 3.175 mm diameter cup was cut 0.38 mm into the rod end as seen in Figure 10 (a) and (b).

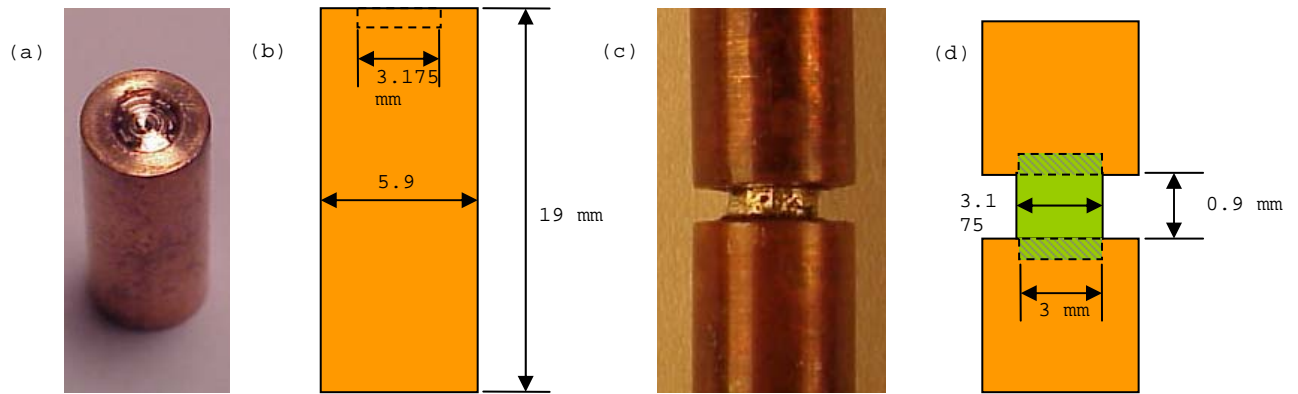


Figure 10. (a) Picture and (b) schematic of Cu rod used in cylinder-type joints. (c) and (d) show the assembled cylinder-type joint.

Following machining the rods were cleaned in a 15% sulfuric acid solution for 30 seconds. After rinsing with distilled water and then methanol, flux was applied into the recessed cup. Monolithic solder disks with a volume larger than the rod's recessed cup were placed in the cups to be reflowed. Together the rods and solder disks were placed on an aluminum plate in a convection oven set at 259°C (532K) air temp, with the cup end orientated upward. The rods were pulled from the oven after 6 minutes and quenched in water. The rods were then cleaned with methanol and a small dab of flux applied on the reflowed solder. This step filled the cupped ends with solder, and prevented air from being trapped in the rods when the cups were oriented downwards in latter assembly. Early samples that were sectioned revealed air cavities trapped in the upper cup and their data was deemed invalid. This step had eliminated this and no further sectioned joints demonstrated this weakness.

The mold in Figures 11 (a & b) was designed and machined specifically for this joint. It consisted of two halves that had a through hole to accommodate the rods and two 'C' shaped aluminum 'C-spacers' 0.9 mm thick. The C-spacers were added to constrain the solder within the joint upon reflow. The cylindrical chamber formed between the C-spacers was 3.175 mm in diameter; hence the cylindrical joints were 3.175 mm in diameter by 0.9 mm in length between copper rods.

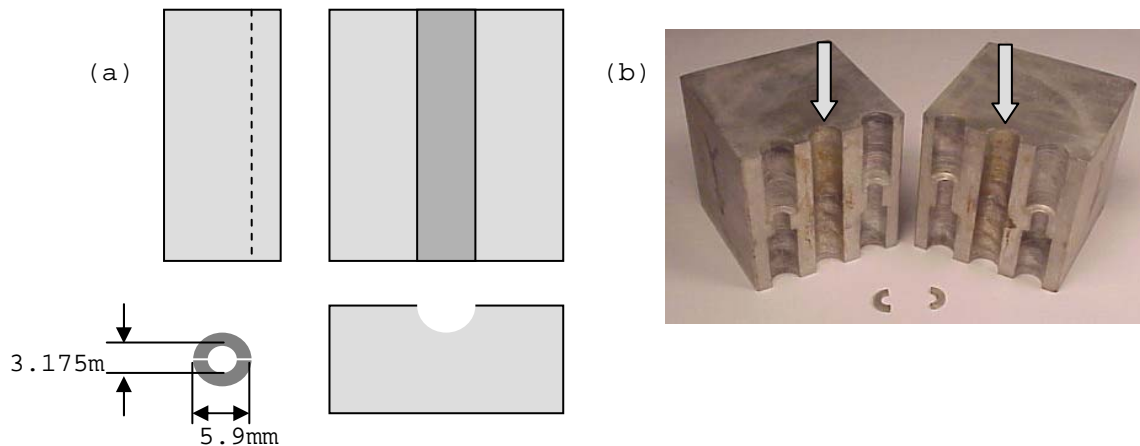


Figure 11. (a) Schematic and (b) picture of mold and C-shapes for cylinder-type joint.

To assemble the cylindrical joints the rods were placed into one half of the mold with a C-spacer between them. A series of monolithic solder disks or a SFC reinforced cylinder was placed in the cutout of the C-spacer and the gap closed with the second C-spacer. The mold halves were then clamped together. The copper rods together with the C-spacers were longer than the mold, this allowed for a weight to be placed on the upper rod. The weight provided a clamping pressure on the C-spacers trapped between the rods. This greatly reduced any leak-by of solder from the intended molded shape. The mold and

weight were heated for 16 minutes in the convection oven at 259°C (532K) air temp. It was found that the solder had not reflowed after 10 minutes, yet 16 minutes resulted in complete reflow; dwell time was estimated at 2-3 minutes.

For cooling the mold was pulled from the oven and placed over a deep sink. Water was slowly poured over the mold till cool to the touch. The mold was then separated and the C-spacers removed from between the rods. A cylindrical joint was then ready for testing.

D. APPARATUS FOR TMC

As the words thermomechanical cycling (TMC) imply, a sample must undergo a thermodynamic cycle as well as a mechanical cycle of stress and strain. In this study the thermodynamic cycling was accomplished by physically cycling a sample from a furnace to a cooler on a repeating time interval. Figure 12 shows the apparatus minus the data acquisition equipment and chill water unit. The furnace was maintained at 180°C (453K) by a closed loop controller while a chill water unit provided water/ethylene glycol chill water mixture at 0°C (273K) to the coils in the cooler section mounted on the underside of the furnace. A pneumatic ram was used to move the sample from cooler to furnace and back. Air for the ram was directed to the top or bottom of the ram by two solenoid valves connected to a timer. The timer was programmed to cycle the solenoid valves and thus the thermodynamic cycle, hourly. To achieve the desired temperature excursions the cycle included 29 minutes inside the furnace with the remaining 31 minutes in the cooler section.

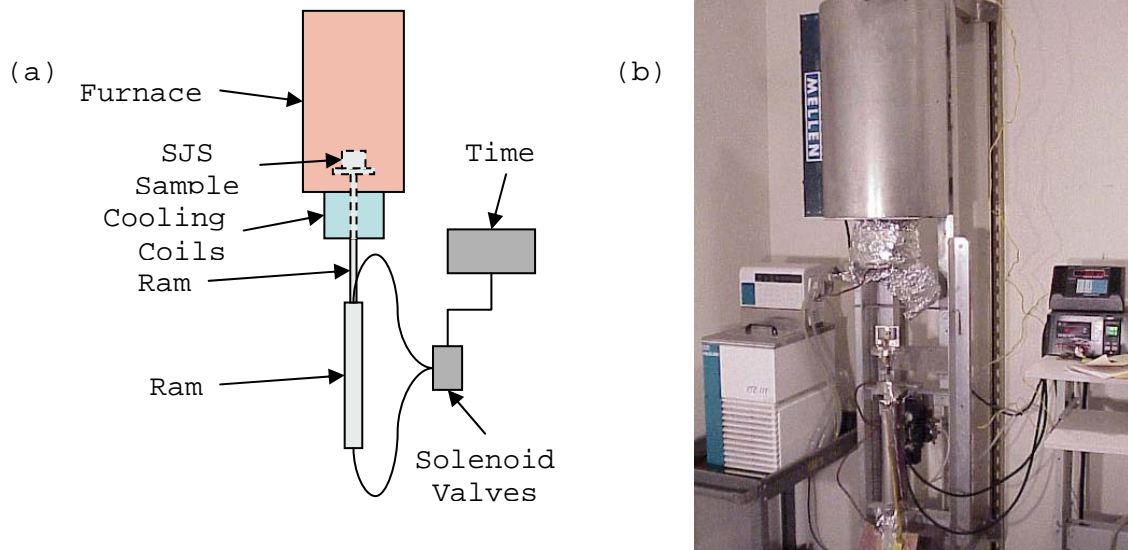


Figure 12. (a) schematic and (b) picture of the Thermomechanical Cycling Apparatus

The fixture used to stress the SJS joints was derived from the bimetallic frame design of Ref (7) and used previously in Refs [8-9]. The frame is illustrated in Figure 13. In using this frame the thermodynamic cycle resulted in the mechanical cycle in the same manner as in FC microelectronic devices. As the temperature of the frame increased the metals expanded based on their own coefficient of thermal expansion (CTE), α , using $\delta = \Delta\alpha \cdot \Delta T \cdot L_0$. The temperature was read from a thermocouple placed in a dimple into the aluminum frame. The initial length, L_0 , was measured from the base to the sample center. This mimics a FC device where distance is measured from the device neutral point (DNP) to the solder joint center. By virtue of the large difference in CTE ($\alpha_{Al} = 2.28 \times 10^{-5} \text{K}^{-1}$) vs. ($\alpha_{inv} = 7.20 \times 10^{-7} \text{K}^{-1}$) the Al columns would expand upward more than

the Invar (lower) grip, and therefore a shear force was applied to the sample at even modest changes in temperature.

If the sample were completely compliant and did not resist shear, the difference in expansion above would give the displacement of the joint in shear. However, the samples did resist shear and this caused stress and strain in the frame. The columns were assumed to be infinitely stiff in comparison to the top beam and all strains caused by the shear forces were assumed to be seen in deflection of the beam. This deflection was measured in volts by four strain gauges placed in pairs on the beam on either side of the upper grip. They were configured electrically in a full Wheatstone bridge. A 10VDC power supply provided excitation while a signal conditioner amplified the output 1000X. To calculate the deflection in millimeters the strain gauge voltage was multiplied by a constant of the beam stiffness, $C = 0.1113 \text{ mm/V}$ [20].

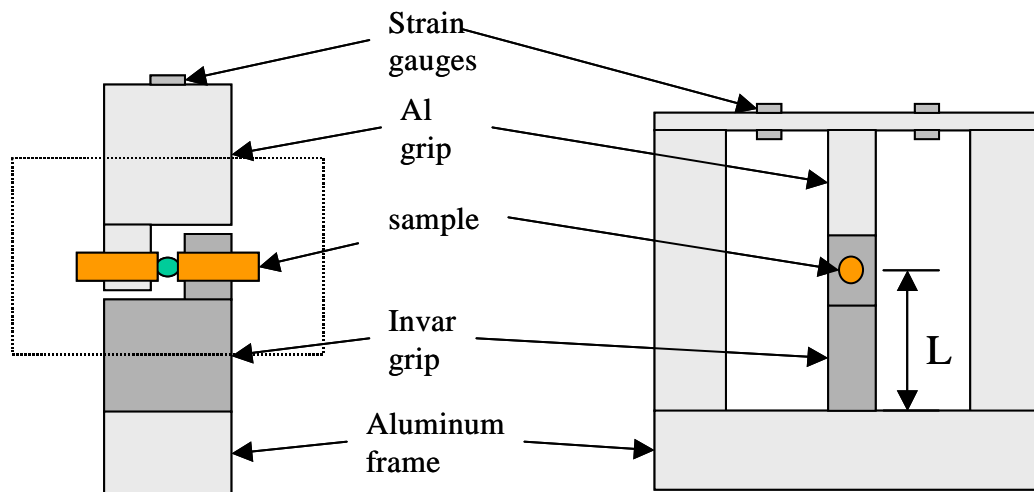


Figure 13. Bimetallic loading frame

E. DATA AND EQUATIONS

In order make use of the information available from the cycling of samples the proper data acquisition must take place. In this study four data points were recorded on a computer during cycling: time, strain gage Nr 1 voltage, strain gage Nr 2 voltage and frame temperature. The time was recorded in clock time at one second intervals and then converted to counting seconds with start being zero. The strain gage voltages were recorded in voltage output for later manipulation. As previously mentioned, the temperature was measured by a K-type thermocouple placed in a dimple in the aluminum frame. It was assumed that any difference between frame and sample temperature was negligible.

Constants that were used throughout the data manipulation were taken from various sources. The coefficients of thermal expansion are examples of known quantities pulled from text. Lengths and areas used in calculations were measured by the author. The loading frame used in this study was the same as used by Marshall [20]. The extensive experimentation to quantify the properties of the loading frame were not repeated and the constants derived by the author of Ref [20] were used in this study.

The shear force on the solder joint was calculated for any given time by the deflection of the beam at that time:

$$P = V/X \quad (1)$$

Where V was the strain gage voltage output and X was the constant $X = 0.0063$ volt/N. Along with this the deflection of the beam, δ_{mech} , was calculated by:

$$\delta_{\text{mech}} = VC \quad (2)$$

$$\text{or } \delta_{\text{mech}} = P/K \quad (3)$$

Where C was the constant of deflection of the beam in mm per volt output from the strain gages, $C = 0.1113 \text{ mm/V}$.

The calculated difference in length of thermal expansion between the aluminum and Invar was given by:

$$\delta_{\text{mech}} = L_o (T - T_o) (\alpha_{\text{Al}} - \alpha_{\text{Inv}}) \quad (4)$$

Where L_o was the length from the base of the frame to the sample center, DNP, T_o was the temperature at test start, and α_{Al} and α_{Inv} were the commonly used coefficient of thermal expansions of aluminum 6160 and Invar respectively.

Shear stresses in the joints were then addressed with:

$$t_{\text{joint}} = P/A \quad (5)$$

$$t_{\text{joint}} = (\delta_{\text{mech}} K) / A \quad (6)$$

Inserting equation (3) into equation (5) returned (6), where K was the stiffness of the frame and A was the area of the solder joint in the shear plane.

The shear strains were then calculated:

$$\gamma_{\text{therm}} = (L_o \Delta T \Delta \alpha) / t_{\text{joint}} \quad (7)$$

$$\gamma_{\text{mech}} = \delta_{\text{mech}} / t_{\text{joint}} \quad (8)$$

$$\gamma_{\text{solder}} = \gamma_{\text{therm}} - \gamma_{\text{mech}} \quad (9)$$

where γ_{solder} was the shear strain in the solder joint. It was calculated by determining the strain due to thermal expansion of the loading frame if the solder joint were compliant. Then the deflection in the top beam of the frame was subtracted to account for the fact that the solder joint did resist the shear.

The strain of the solder joint was then divided into elastic and inelastic to get a clearer view of the reactions of the solder joint to the imposed strains.

$$\gamma_{\text{elastic}} = \tau_{\text{joint}}/G \quad (10)$$

$$\gamma_{\text{inelastic}} = \gamma_{\text{solder}} - \gamma_{\text{elastic}} \quad (11)$$

The data was imported into an Excel file for the above equations to be worked. This calculated data was then imported to Kalidegraph for graphing into visually meaningful representations.

F. MICROSCOPIC OBSERVATION

The process of putting the SJS joints into pucks for microscopy was the same regardless of joint type. In each case the assembled joints were too long for the puck molds and had to be trimmed. The assembled joints were placed in the fixture used to assemble the Ball-type SJS joint; this was done to provide adequate support and to not cause damage to the sample during cutting. The fixture was then easily clamped onto the arm of a diamond-wafering saw. Cutting was done in two passes, one on either rod, with approximately 6 mm being removed in each pass. The joint was then placed in the puck mold and the Buehler Sample-Quick acrylic puck material poured in. After hardening the samples were easily removed from the molds in an easy to handle package ready for polishing.

The polishing regime for all samples started with wet sanding using 320 grit silicon carbide paper. This large grit was needed to get quickly to the center of the samples. Following 320 grit: 500, 800, 1000, 2400 and 4000 grits were used successively. Diamond suspensions of 6 micron and 1 micron preceded the final mirror polish using 0.05 micron colloidal silica.

Pucks of this form may have provided for an easy to handle sample for optical microscopy, but electrically insulated the sample, making SEM evaluation impossible. In order to use the SEM the back side of the puck was ground away in the same fashion as before until copper of the rods was exposed. Thus, a conductive path was then opened to allow electron microscopy. A SEM was used for elemental mapping using Link ICIS software.

THIS PAGE INTENTIONALLY LEFT BLANK

V. RESULTS AND CONCLUSIONS

A. THERMOMECHANICAL CYCLING

Shown in Figure 14(a) is the average joint shear stress ($\bar{\tau}$) versus temperature (T) for the 12th thermo-mechanical cycle (TMC) of the monolithic and the Cu/Cu₆Sn₅ reinforced solder ball-type joints. The 12th cycles are plotted to ensure stable stress/strain hysteresis behavior had developed, previously found to take between 3-5 cycles [21]. The plots begin with the joints in stress-free states (25°C, 298K) and increase elastically (linear) with temperature till high temperature creep mechanisms are initiated at approximately 70°C (343K). From this point the plots are non-linear due to the stress-relief the creep provides. As the samples cool, stress is again built up until around 80°C (353K), when the joints yield plastically with large strain localization in shear bands; this allows the stress to return to a near zero value. The stress within the shear bands must be considerably greater than the average stress plotted as the plotted stress at initiation of plasticity is lower than the yield strength of the solder.

As seen in Figure 14(a), the behaviors of the monolithic solder and the 7 vol. % Cu/Cu₆Sn₅ reinforced solder are nearly identical in geometry. This implies that the passive reinforcement has little impact on the thermo-mechanical behavior at this small vol. percentage. Of note, this plot shape is similar in geometry to previous studies of Pb-Sn solders [21].

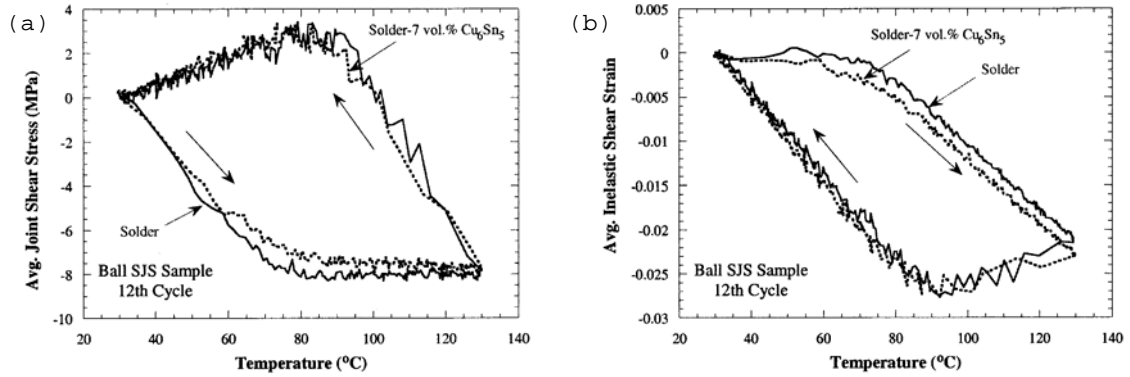


Figure 14. a) $\bar{\tau}$ vs. T , b) $\bar{\gamma}$ vs. T . for the 12th cycle of the monolith and Cu reinforced ball-type SJS joints.

The average inelastic shear strain ($\bar{\gamma}$) vs. temperature (T) during the 12th TMC is shown in Figure 14(b) for the monolith and Cu/Cu₆Sn₅ reinforced solder ball-type joints. The hysteresis loops form in a clockwise fashion as the samples are heated. Initially the joints are loaded elastically and no inelastic strain is evident. Then the plastic strains develop sharply at 67°C (340K) as high temp creep mechanisms become active. During cooling the strains return to near zero. As seen with the average shear stress plot in Figure 14(a) there is little difference between the monolithic and reinforced solders. This substantiates that the effect of the Cu/Cu₆Sn₅ passive reinforcement in small volume percentages is minimal.

The average shear stress ($\bar{\tau}$) vs. temperature (T) is plotted in Figure 15(a) for the 12th cycle of the cylindrical samples of monolithic solder and 11 vol. % NiTi single-fiber composite (SFC) reinforced solder. It is seen that stress in the SFC sample builds more rapidly and sustains a higher value than the monolith during heating. This is made evident at approximately 70°C (343K) where the

stress in the monolith begins to level off, where as the SFC sample continues to build and experience an overall greater range of stress through the cycle. The average shear strain ($\bar{\gamma}$) vs. temperature (T) for the cylindrical monolith and SFC samples is plotted in Figure 15(b). Differences in behavior are apparent throughout nearly the entire temperature range of the cycle. For the initial 30°C (303K) of heating the strain in both samples is elastic and no difference is discernable. It is after this initial elastic region that the behavior differs. The monolith sample develops a higher strain rate and ultimately a greater total inelastic strain. Both samples returned to near zero strain at the completion of the cycle, therefore the monolith experiences a greater range of strain, $\Delta\gamma_{\text{inelastic}}$. The fact that the SFC solder develops less $\Delta\gamma_{\text{inelastic}}$ could be a major benefit, as it should enhance its low cycle fatigue life relative to the monolith.

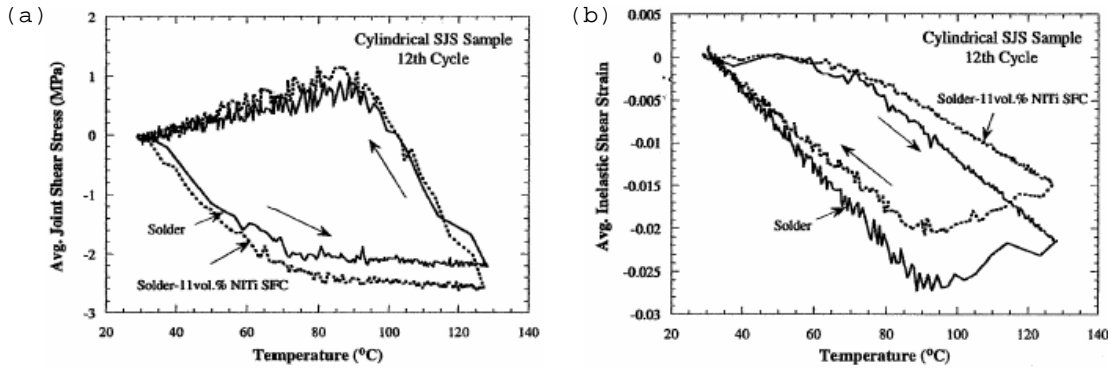


Figure 15. a) $\bar{\tau}$ vs. T, b) $\bar{\gamma}$ vs. T. for the 12th cycle of the monolith and SFC reinforced cylindrical-type SJS joints.

The plots of average shear stress ($\bar{\tau}$) vs. temperature (T) and average inelastic shear strain ($\bar{\gamma}_{\text{inelastic}}$) vs. temperature (T) are shown in Figures 16(a & b) for the 1st cycle of the cylindrical monolith and SFC samples comparatively. The basic trend of both plots is similar to those for the 12th cycle; the SFC has a larger shear stress range and a resulting smaller inelastic strain range, however, there are differences. It is when comparing the 1st and 12th cycle $\bar{\tau}$ vs. T behavior of the monolith and SFC samples together do the differences become apparent. As the SFC sample cools during the 1st cycle a 'knee' develops in the plotted $\bar{\tau}$ vs. T. This is absent in the 12th cycle of the SFC and never appears in the monolith at any cycle. This suggests that the monolith experiences stress localization much easier than the SFC, as seen by the lower $\bar{\tau}$ level.

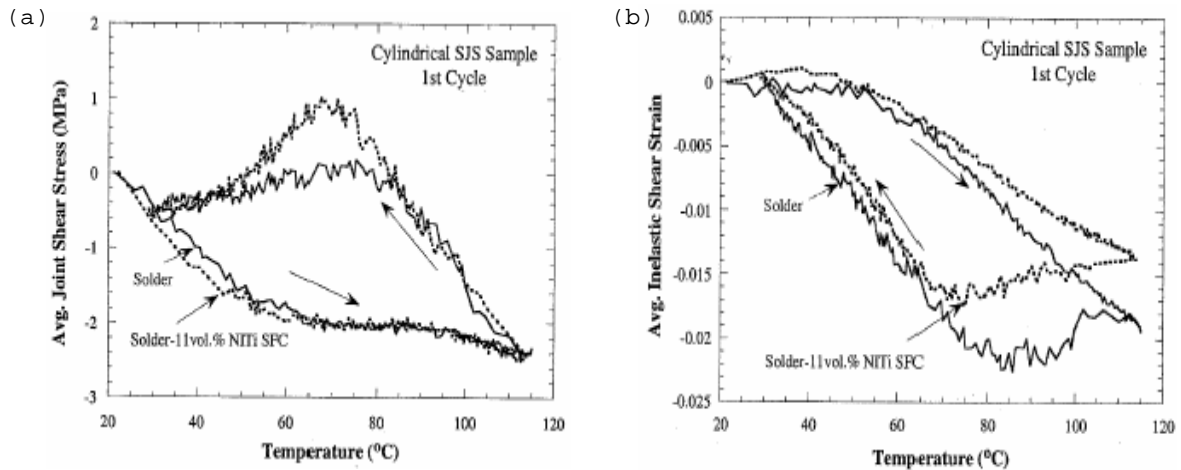


Figure 16. a) $\bar{\tau}$ vs. T, b) $\bar{\gamma}$ vs. T. for the 1st cycle of the monolith and SFC reinforced cylindrical-type SJS joints.

Comparison of the 1st and 12th cycles of the monolith and SFC reinforced cylindrical-type joints, Figures 15 & 16, reveals possible benefits in the SFC. While the $\bar{\tau}_{\max}$ experienced by the joints are similar for the monolith and SFC (approximately 18% greater in the SFC than the monolith in the 12th cycle, indiscernible in the 1st cycle) the maximum inelastic strain in the SFC is smaller than the monolith in both cycles. This nearly 26% reduction in inelastic strain range is the obvious benefit to solder life within microelectronic devices; the reduced strain range should coincide with a decrease in LCF failures. The reduced strain range did not come with an increase in counterproductive stresses to be applied to the microelectronic devices (Si or GaAs chips), adversely affecting the likelihood of their failure.

It certainly appears that NiTi reinforcement results in some benefits, during the 1st cycle, most notably, where the inelastic strain range was substantially reduced without a corresponding increase in maximum stress. To explain such behavior and the differences between 1st and 12th cycle behaviors the phase transition behavior of the NiTi was examined by differential scanning calorimetry (DSC).

B. DIFFERENTIAL SCANNING CALORIMETRY

Figure 17 shows the DSC scans of a NiTi wire sample in two runs of different temperature ranges: (a) -35°C to 80°C (238K to 353K), (b) 10°C to 75°C (283K to 348K). In both runs the sample was cooled to the initial temperature and held there for 5 minutes before the scan was initiated. Once reaching maximum temperature the sample was held for 5 minutes at this temperature before cooling. The heating

and cooling rates ($10^{\circ}\text{C}/\text{min}$, $283\text{K}/\text{min}$) were constant and equal throughout both scans. The weight of both samples was approximately 40 mg.

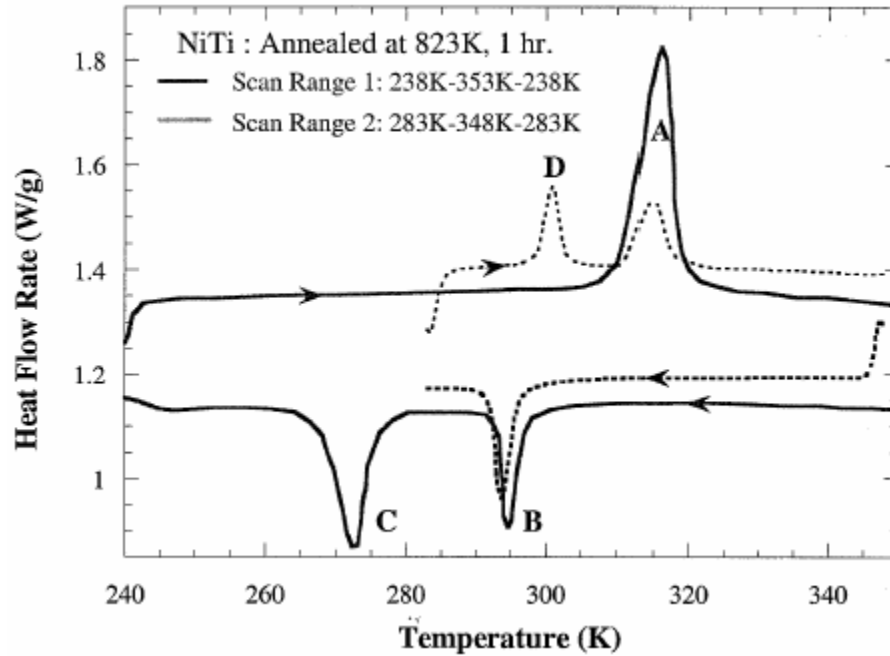


Figure 17. Two DSC scans of NiTi samples over dissimilar temperature ranges.

In the first scan during equilibration at -35°C (238K) the entire sample material was transformed into the martensitic B19' phase (triagonal structure). During heating, a single exothermic peak, A, occurs at 43°C (316K). This corresponds to the transformation from B19' to B2 phase (ordered BCC phase), after this peak the entire material has transformed to single phase B2. In contrast to the heating, when cooling two peaks (B and C) were seen, but both were endothermic. Eggeler et al [22, 23] have demonstrated via use of transmission electron microscopy (TEM) and DSC that the first peak, B, at 22°C (295K), is the transformation of B2 into a two phase mixture of B19'

and rhombohedral martensitic phase, R. R is the majority phase at approximately 70 percent by volume, with B19' the minor. The second peak, C, occurs at 0°C (273K), this is the transformation of the R phase constituent to the B19', thus returning the sample to a single B19' phase material. This two-stage transformation is indicative of Ni₄Ti₃ precipitates present in the microstructure. The precipitate/B2 interfaces promote the nucleation of the R and B19' phases during cooling, as seen in the scan [22]. Prior to the DSC scans the samples were annealed at 550°C (823K) for 1 hour so Ni₄Ti₃ precipitates are expected.

The second scan shows very different behavior. From the first scan we can see that at 10°C (283K) the R and B19' phases will coexist (with R in the majority), as well as Ni₄Ti₃ precipitates. In heating from the second scan's starting temperature of 10°C (283K) two exothermic peaks occur. The first peak, D, at 28°C (301K) corresponds to the transformation of R to B2, thus the microstructure now consists of both B2 and B19' phases. As in the first scan the B19' transforms to B2 at 43°C (316K) (peak A), however, in this scan the volume percent of B19' is approximately 30%, resulting in this second exothermic peak being significantly smaller. Cooling to 10°C (283K), the B2 transforms to the R/B19' mixture at B, but does not become single phase B19'. Recalling that to become single B19' phase the sample needed to be cooled below 0°C (273K) (peak C).

From the two scans together we can see that at room temperature the two-phase microstructure (R/B19') is expected after annealing as the samples were not cooled past room temperature. When casting the solder with SFC

reinforcement the samples are heated to greater than 250°C (523K) and then rapidly cooled to room temperature. The SFC will then be the martensitic R/B19' microstructure when the TMC's are initiated. As a result, during the 1st TMC the martensite-to-austenite transformation occurs over the range corresponding to peaks A and D, 23-50°C (296-323K). During the TMC cycling the samples' temperatures only return to around 30°C (303K), which is higher than either peak B or C. This means that no phase transformation will occur during cooling and the SFC is now effectively maintained in the B2 microstructure. Therefore, the NiTi would behave as a passive reinforcement with a constant stiffness in later cycles, in contrast to the 1st cycle where the fiber behaves as an 'adaptive' or 'smart' reinforcement.

C. SHAPE MEMORY EFFECT

Figure 18 compares the average inelastic shear strain vs. temperature for the 1st and 12th cycles over the limited temperature range: 20-60°C (293-333K). The martensite-to-austenite transformation temperature range is marked by arrows P and Q. It can be easily seen that the inelastic shear strain for the 1st cycle actually increases in a positive magnitude initially before decreasing and becoming increasingly negative as the temperature rises. The 12th cycle exhibits no such behavior. Here the inelastic shear strain merely maintains near zero before increasing negatively once approximately 50°C (323K) is reached. From the DSC it's deduced that this difference in behavior results from difference in the temperatures at the cycle start. The 12th cycle returns to just under 30°C (303K) before reheating, vice 20°C (292K). This leaves the NiTi in an austenitic state throughout the cycle. As a result

the SFC reinforcement acts as a stiffener internal to the solder ball and the inelasticity is delayed. In contrast, the 1st cycle has been at room temperature prior to cycling and is not completely austenite, as explained in the cooling of the second DSC scan. As the martensite does transform to austenite we see the reverse inelasticity (i.e., the strain in opposite direction of applied force) in the beginning moments of the cycle. As the solder joint is strained in the positive direction the NiTi fiber is in turn strained as well. During the 1st cycle, this is countered by a strain due to the shape memory effect. This strain places the solder matrix surrounding the NiTi in a positive strain state as seen the in the initial rise in Figure 18. The transformation is completed by 50°C (323K) and the joint deforms with the applied stress and the inelastic strain becomes negative.

The impact of the shape-memory effect of the NiTi reinforced solder composites is not completely clear, however, it appears that it is possible to obtain the desired reverse shear deformation; by first deforming the solder and fiber and then using the shape recovery of the NiTi over the austenite-martensite transformation temperature range.

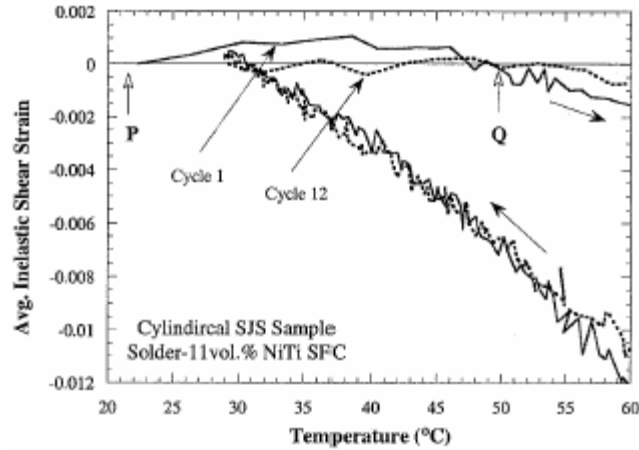


Figure 18. $\bar{V}_{\text{inelastic}}$ vs. T for 1st and 12th cycles of SFC over limited range.

D. MICROSTRUCTURE

Figure 19(a) shows a monolithic SnAgCu solder Single-Joint-Shear (SJS) ball type joint used in this work. The ball is approximately 2 mm in diameter joining two 5.9 mm Cu cylinders and sits on a pad 1.6 mm in diameter raised 0.1 mm from the surrounding Cu surface. This geometry was chosen to simulate the morphology of the ball grid array (BGA) or flip-chip (FC) joints. A sample of this joint was thermomechanically cycled 48 times and then sectioned and polished for evaluation. The resulting microstructure can be seen in Figures 19(b) and (c) at 750X and 3000X magnifications respectively. The figures clearly show that the microstructure is primarily β -Sn regions of approximately 10 μm grain size and then between these grains are areas with divorced eutectic particles of fine Ag_3Sn . The eutectic particle size averages $\leq 0.5 \mu\text{m}$. Cu_6Sn_5 is present in small quantities throughout the material as well.

The microstructure of a monolithic SJS sample after 96 thermo-mechanical cycles is seen in Figures 20(a) and (b), again under 750X and 3000X magnification. When comparing the 48 cycle to the 96 cycle microstructure the primary β -Sn grain size appears slightly larger (15 μm vice 10 μm) but there is little difference in the Ag_3Sn particle size.

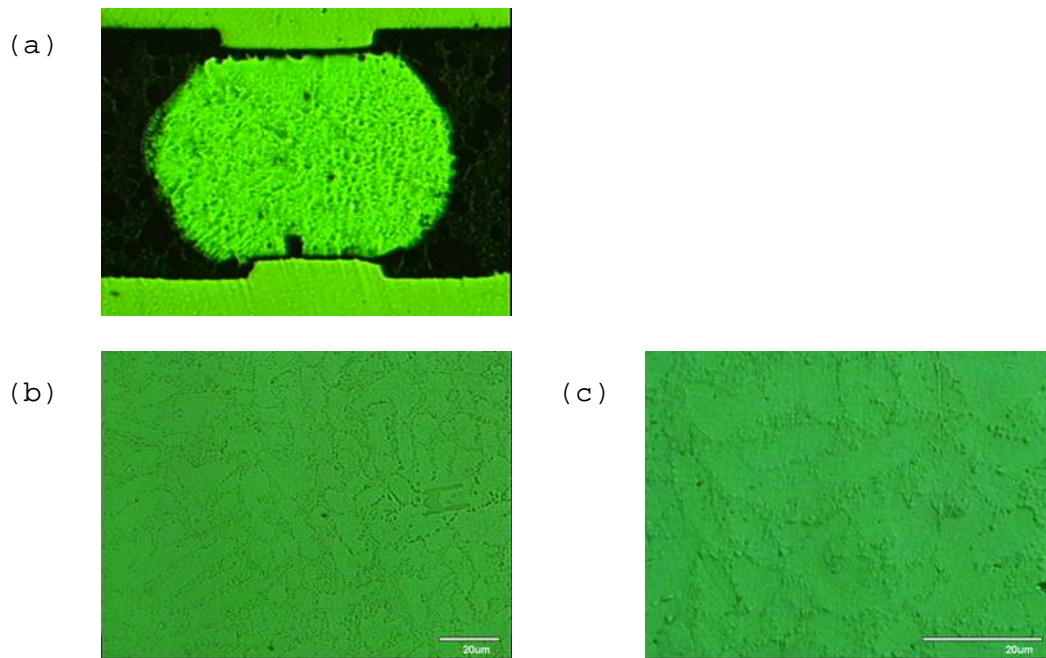


Figure 19. SnAgCu SJS ball joint (a) overview, (b) & (c) microstructure after 48 TMC at 750X and 3000X.

The variance in the β -Sn grain size could be a result of either slight differences in solidification rates or dwell times during reflow. More samples of each would be needed to conclude that the grain size increase is a direct result of phase coarsening do to the TMC.

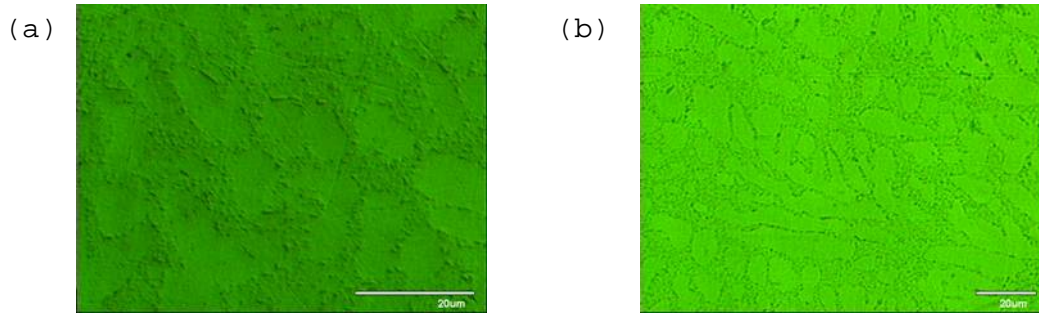


Figure 20. SnAgCu microstructure after 96 TMC, (a) 1500X, (b) 3000X

Figures 21(a-c) show the microstructure of the same SJS ball type joint of SnAgCu solder but this time with 7% vol. Cu/Cu₆Sn₅ reinforcement. The reinforcement was spheroidal Cu particles between 5-10 μm in diameter. These particles would react with the Sn matrix and become Cu₆Sn₅ intermetallics at the interfaces. In Figure 21(a) the Cu₆Sn₅ can be seen surrounding the remaining Cu along the particle-matrix interface. Figure 21(b) shows that the particles of Cu and Cu₆Sn₅ were uniformly distributed throughout the β -Sn matrix, though usually trapped along the grain boundaries as seen in Figure 21(c). Also from Figure 21(c) we can see that often the Cu particles are completely consumed and the conversion to Cu₆Sn₅ is complete. Because the matrix does not appear changed between the monolith and reinforced solders the testing should reveal the role of the reinforcements in strain response.

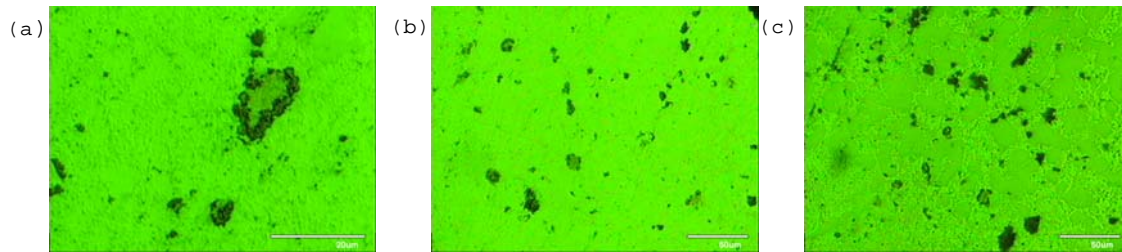


Figure 21. Cu/Cu₆Sn₅ reinforced ball-type SJS joints under magnification. (a) Cu/Cu₆Sn₅ conversion at interfaces, (b) uniform dispersion of reinforcements within matrix, (c) reinforcements located at the matrix grain boundaries.

Photographs of the SFC reinforced samples reveal the microstructure of the matrix, Figure 22(a) and the SFC/matrix interface, Figure 22(b). The microstructure of the matrix is seen to not vary from the monolith cylinder microstructure. This leads to the conclusion that any variance in stress response of the samples can be concluded to be a result of the SFC reinforcement. In Figure 22(b) the Ni₃Sn₄ intermetallic layer that formed at the SFC/matrix interface during reflow shows that use of the HF based flux satisfactorily solved wetting problems experienced with other fluxes.

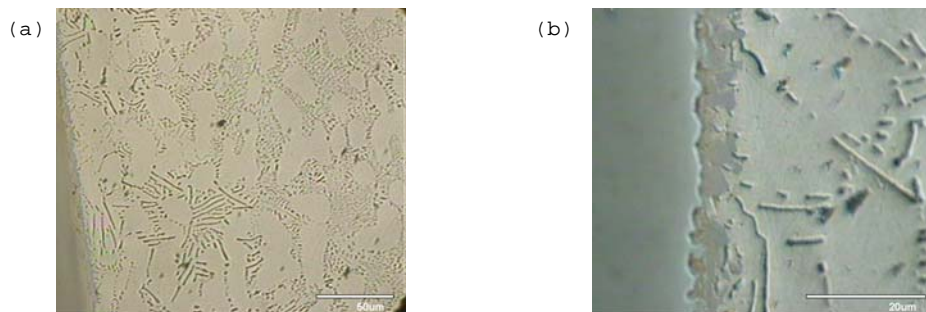


Figure 22. NiTi SFC reinforced cylindrical-type SJS joints. (a) solder matrix, (b) Ni₃Sn₄ layer formed at the interface of the SFC and matrix.

THIS PAGE INTENTIONALLY LEFT BLANK

VI. SUMMARY

In this study, solder joints were tested by TMC in an effort to compare a monolith solder to 2 composite solders. This was undertaken to try and reduce effects with the solders joints that cause failure due to low cycle fatigue in FC and BGA devices. A SnAgCu monolith solder was tested as a baseline, and then compared to a Cu/Cu₆Sn₅ particulate reinforced solder as well as a NiTi SFC reinforced solder. The NiTi testing was in attempt to show the possibility of placing a shape memory alloy within a solder joint that would provide a mechanism for the joints to actively resist inelastic deformation.

Copper powder was successfully added to the solder matrix at 7% vol. and then formed into bulk solder. This reinforced solder was tested and compared to the monolith solder in ball-type joints of similar form to FC or BGA solder balls. Analysis showed that the behavior of the different solders under TMC were very similar. In the limited scope of this study no benefits were seen from the copper reinforcements at this low volume percent reinforcement.

The NiTi reinforced solder was also tested and compared to a monolith, however, in the form of cylindrical shaped joint that did not model an actual solder ball, but was useful for comparison of materials. The addition of the shape memory alloy was shown to resist deformation by way of martensite to austenite phase transformation. Reverse shear was seen at the onset of the phase transformation and reduced strain range over the monolith throughout the cycle was achieved. This demonstrated that

the shape memory effect could be used to actively reinforce solder joints in such a way as to reduce low cycle fatigue. The reduced strain range of a joint supported that this was achieved. Recently, Dutta, Majumdar and Wang using different methodology achieved similar results [28]. Thus further supporting the conclusions here.

Through the use of DSC and analysis of TMC data the shape memory effect can clearly be seen to be of benefit, but also where it must be improved. The martensite to austenite phase transformation that was useful to our purpose was in the wrong temperature range to be useful in actual electronic devices. Refinement of the shape memory alloys to raise the transition temperature to above normal ambient temperatures should allow its use in practical applications.

LIST OF REFERENCES

1. The International Technology Roadmap for Semiconductors, Semiconductor Industry Association, San Jose, CA, 1999.
2. J. L. Marshall and J. Calderon, "Hard-particle Reinforced Composite Solders Part 1: Microcharacterisation," *Soldering & Surface Mount Technologies*, No. 26, pp. 23-29 (1997).
3. A. W. Gibson, K. N. Subramanian and T. R. Bieler, "Comparison of Mechanical Fatigue Fracture Behavior of Eutectic Sn-Ag Solder With and Without Cu_6Sn_5 Intermetallic Particulate Reinforcement," *Journal of Advanced Materials*, Vol. 30, No. 2, 1998, pp. 19-24.
4. J. Sigelko, S. Choi, K. N. Subramanian, J. P. Lucas and T. R. Bieler, "Effect of Cooling Rate on Microstructure and Mechanical Properties of Eutectic Sn-Ag Solder Joints with and without Intentionally Incorporated Cu_5Sn_6 Reinforcements," *Journal of Electronic Materials*, Vol. 28, No. 11, pp. 1184-1188, (1999).
5. F. Guo and K.N. Subramanian, "Solders strengthened with copper and silver particles," *Advanced Materials & Processes*, pp. 10-12, Dec. 2002.
6. I. Dutta, "A Constitutive Model for Creep of Lead-Free Solders Undergoing Strain-Enhanced Microstructural Coarsening: A First Report," *Journal of Electronic Materials*, Vol. 32, No. 4, pp. 201-207, (2003).
7. P. L. Hacke, Y. Fahmy and H. Conrad, "Phase Coarsening and Crack Growth Rate During Thermo-Mechanical Cycling of 63Sn37Pb Solder Joints," *Journal of Electronic Materials*, Vol. 27, No. 8, pp. 941-947, (1998).
8. X. Q. Shi, Z. P. Wang, W. Zhou, H.L.J Pang, and Q. J. Yang, "A New Creep Constitutive Model for Eutectic Solder Alloy," *Journal of Electronic Packaging*, Vol. 124, pp. 85-90, June 2002.

9. P. Hacke, A. F. Sprecher, and H. Conrad, "Computer Simulation of Thermo-Mechanical Fatigue of Solder Joints Including Microstructure Coarsening," *Journal of Electronic Packaging*, Vol. 115, pp. 153-158, June 1993.
10. X. Liu and G. Q. Lu, "Effects of Solder Joint Shape and Height on Thermal Fatigue Lifetime," *IEEE Transactions on Components and Packaging Technologies*, Vol. 26, No 2, pp. 455-465, June 2003.
11. J. H. L. Pang, D. Y. R. Chang and T. H. Low, "Thermal Cycling Analysis of Flip-Chip Solder Joint Reliability," *IEEE Transactions on Components and Packaging Technologies*, Vol. 24, No 4, pp. 705-712, Dec 2001.
12. X. Q. Shi, J. L. J. Pang, W. Zhou, and Z. P. Wang, "Low cycle fatigue analysis of temperature and frequency effects in eutectic solder alloy," *International Journal of Fatigue*, Vol. 22, pp. 217-228, (2000).
13. National Institute of Standards and Technology and Colorado School of Mines, *Database for solder Properties with Emphasis on New Lead-Free Solders*, Table 1.11, Colorado, 11 February 2002.
14. Official Journal of the European Union, Directive 2002/95/EC of the European Parliament and of the Council of 27 January 2003 on the restriction of the use of certain hazardous substances in electrical and electronic equipment," 13 February 2003.
15. M. Abtew and G. Selvaduray, "Lead-free Solders in Microelectronics," *Materials Science and Engineering*, 27, pp. 95-141, (2000).
16. International Electronics Manufacturing Initiative, "NEMI Group Recommends Tin/Silver/Copper Alloy as Industry Standard for Lead-Free Solder Reflow in Board Assemblies,"
[<http://www.inemi.org/cms/newsroom/PR/2000/PR012400.html>], 24 January 2000.

17. D. E. Hodgson, M. H. Wu, and R. J. Biermann, "Shape Memory Alloys," [http://www.jmmedical.com/html/_shape_memory_alloys.html], July 2006.
18. D. Mantovani, "Shape Memory Alloys: Properties and Biomedical Applications," *Journal of Metals*, Vol 52, No 10, pp. 36-44, October 2000.
19. "NiTi Medical Technologies Awarded the CE mark for its flagship surgical device," The Israeli Healthcare, Biotech and Pharma Newsletter, Israel International Export and Cooperation Institute, No 1, May 2004.
20. C. Marshall, *Thermomechanical Cycling of Flip Chip Solder Joints with and without Underfill Encapsulant*, Master's Thesis, Naval Post Graduate School, Monterey, California, December 2001.
21. I. Dutta, A. Gopinath and C. Marshall, "Underfill Constraint Effects during Thermomechanical Cycling of Flip-Chip Solder Joints," *Journal of Electronic Materials*, Vol. 31, No. 4, pp.253-264, (2002).
22. J. Kjalil-Allafi, A. Dlouhy and G. Eggeler, "The mechanism of multistage martensitic transformations in aged Ni-rich NiTi shape memory alloys," *Acta Materialia*, 50, pp. 793-803, (2002).
23. G. Eggeler, J. Khalil-Allafi, K. Neuking and A. Dlouhy, *AZ. Metallkd.*, 93, 2002, pp. 654-660.
24. J-H. Lee, D-J. Park, J-N. Heo, Y-H. Lee, D-H. Shin and Y-S. Kim, "Reflow Characteristics of Sn-Ag Matrix In-Situ Composite Solders," *Scripta Materialia*, 42, pp. 827-831, (2000).
25. W. Yang, R.W. Messler, and L. E. Felton, "Microstructure Evolution of Eutectic Sn-Ag Solder Joints," *Journal of Electronic Materials*, Vol. 23, No. 8, pp. 765-772, (1994).
26. F. Guo, S. Choi, J. P. Lucas, and K. N. Subramanian, "Effects of Reflow on Wettability, Microstructure and Mechanical Properties in Lead-Free Solders," *Journal of Electronic Materials*, Vol. 29, No. 10, pp. 1241-1248, (2000).

27. C. Pfeiffer, C. Mavroidis, K. DeLaurentis and M. Mosley, Shape Memory Alloy Actuated Prothesis: Initial Prototypes,
<http://www.robots.neu.edu/papers/lmece99.PDF>, July 2006.
28. 28. Z.X. Wang, I. Dutta and B.S. Majumdar,
"Thermomechanical response of a lead-free solder reinforced with a shape memory alloy," Scripta Materialia, 54, pp. 627-632, (2006).

INITIAL DISTRIBUTION LIST

1. Defense Technical Information Center
Fort Belvoir, Virginia
2. Dudley Knox Library
Naval Postgraduate School
Monterey, California
3. Professor Indranath Dutta
Department of Mechanical and Astronautical Engineering
Naval Postgraduate School
Monterey, California
4. Department Chairman, Code ME
Department of Mechanical and Astronautical Engineering
Naval Postgraduate School
Monterey, California
5. William A. Horton, III
Carmen Industries
Jeffersonville, Indiana
6. Lieutenant Commander W. Scott Horton
Chula Vista, California
7. Engineer Officer
USS CHANCELLORSVILLE (CG 62)
Naval Station San Diego
San Diego, California